

Accepted for publication in the Astrophysical Journal

## Destruction of Interstellar Dust in Evolving Supernova Remnant Shock Waves

Jonathan D. Slavin

*Harvard-Smithsonian Center for Astrophysics, 60 Garden Street, Cambridge, MA 02138*

`jslavin@cfa.harvard.edu`

Eli Dwek

*Observational Cosmology Lab., Code 665, NASA at Goddard Space Flight Center, Greenbelt, MD 20771, USA*

and

Anthony P. Jones

*Institut d'Astrophysique Spatiale (IAS), UMR 8617, CNRS/Université Paris-Sud, 91405 Orsay, France*

### ABSTRACT

Supernova generated shock waves are responsible for most of the destruction of dust grains in the interstellar medium (ISM). Calculations of the dust destruction timescale have so far been carried out using plane parallel steady shocks, however that approximation breaks down when the destruction timescale becomes longer than that for the evolution of the supernova remnant (SNR) shock. In this paper we present new calculations of grain destruction in evolving, radiative SNRs. To facilitate comparison with the previous study by Jones et al. (1996), we adopt the same dust properties as in that paper. We find that the efficiencies of grain destruction are most divergent from those for a steady shock when the thermal history of a shocked gas parcel in the SNR differs significantly from that behind a steady shock. This occurs in shocks with velocities  $\gtrsim 200 \text{ km s}^{-1}$  for which the remnant is just beginning to go radiative. Assuming SNRs evolve in a warm phase dominated ISM, we find dust destruction timescales are increased by a factor of  $\sim 2$  compared to those of Jones et al. (1996), who assumed a hot gas dominated ISM. Recent estimates of supernova rates and ISM mass lead to another factor of  $\sim 3$  increase in the destruction timescales, resulting in a silicate grain destruction timescale of  $\sim 2\text{--}3 \text{ Gyr}$ . These increases, while not able to resolve the problem of the discrepant timescales for silicate grain destruction and creation, are an important step towards understanding the origin, and evolution of dust in the ISM.

## 1. Introduction

The evolution of dust grains in the interstellar medium (ISM) is governed by the processes of creation, including those that add material to pre-existing grain cores, and destruction, those processes that return grain material back to the gas phase. Grain cores are created by thermal condensation in stellar sources such as the quiescent outflows of asymptotic giant branch (AGB) stars or the explosively ejected material in supernova (SN) events and may grow via cold accretion onto refractory grain cores in the dense ISM. Grains are destroyed by sputtering and vaporization in grain-grain collisions in interstellar shocks. Different processes are important in different interstellar environments with dense environments, such as cold H I clouds and molecular clouds leading primarily to grain growth while lower density environments, such as diffuse, warm ( $T \sim 5000 - 10^4$  K) either ionized or neutral gas, are mainly sites for grain destruction. As has been recognized for many years, the dominant means of destruction for grains is via fast shock waves mostly generated in the ISM by supernova explosions. Grains are destroyed in shocks by a variety of processes (see e.g., Jones et al. 1996, hereafter JTH96) including thermal sputtering, non-thermal (or inertial) sputtering and shattering and vaporization caused by grain-grain collisions. Both the compression in the shock, with the accompanying enhancement of the magnetic field and betatron acceleration of the grains, and the heating of the gas (for non-radiative shocks) act to enhance the sputtering of the grains.

Grain destruction in shocks has been the subject of numerous studies over the past several decades (e.g., Shull 1977; Draine & Salpeter 1979a; Seab & Shull 1983; McKee et al. 1987; Jones et al. 1994, 1996; Dwek et al. 1996; Slavin et al. 2004; Bocchio et al. 2014). In most of these works, the shock profile used was that for a steady, plane parallel shock (though Draine & Salpeter 1979a; McKee et al. 1987, have approximated shock evolution). Dwek (1981) calculated the time-dependent dust destruction in supernova remnants, but only during the Sedov-Taylor phase of their evolution. The rationale for using steady shocks is that the processing timescale is short compared with the evolution timescale for the shock and that the processing occurs within a distance that is small enough that the difference between a plane parallel and spherical shock is negligible. As we show below, neither of these assumptions is completely justified for supernova remnant (SNR) shocks in the warm, low density medium, which is the most important phase in the ISM for grain destruction.

## 2. Methods

To assess the effects of hydrodynamical shock evolution on grain destruction, we have carried out numerical hydrodynamical calculations of supernova remnant (SNR) evolution. We have then used that data to construct shock profiles for many gas parcels for which we have then used our grain processing codes to calculate the evolution of dust contained in those parcels.

## 2.1. Hydrodynamical Calculations

Our hydrodynamical calculations presented here were done with our own code, which is based on (and shares some code with) the VH-1 code (<http://astro.physics.ncsu.edu/pub/VH-1/>), which employs a slightly simplified version of the piece-wise parabolic method of Colella & Woodward (1984). Ours is a 1D code, assuming spherical symmetry and includes several enhancements necessary for our calculations. It uses the same method as VH-1, taking a Lagrangian step, followed by remap onto a fixed grid. The enhancements relative to the VH-1 code include: optically thin radiative cooling, non-equilibrium ionization, thermal conduction and magnetic pressure.

### 2.1.1. Radiative Cooling and Ionization

Radiative cooling is included using a set of look-up tables with cooling rate per ion vs. temperature that were generated using an updated version of the Raymond & Smith code (Raymond & Smith 1977). The cooling rate uses the current ionization state, calculated as described below, and is thus consistent with the ionization, which leads to a large enhancement of the cooling relative to that for collisional ionization equilibrium in the immediate post-shock region where the gas is under-ionized. The elements included in the ionization and cooling rate calculations are H, He, C, N, O, Ne, Mg, Si, S, Ar, Ca, Fe, and Ni. The abundances assumed are those of Grevesse (1984) in order to be in keeping with the plane parallel shock calculations used by JTH96 with which we will compare results. We do not include dust cooling, which affects the pressure in the hot bubble at late times (Dwek 1981). To maintain the temperature in the ambient medium and prevent cooling to temperatures well below  $10^4$  K in the post-shock region, we include a heating rate that balances the collisional ionization equilibrium cooling rate at  $T = 10^4$  K. The heating is turned on only for  $T < 10^4$  K and cooling is turned off for those temperatures. We do not expect this to have any significant effects on the grain destruction because in the cold shell the compression is governed by the magnetic field and thermal sputtering is insignificant at  $T \lesssim 10^4$  K.

The non-equilibrium ionization calculations use collisional ionization and recombination rates from look-up tables generated similarly to the cooling rate tables. We also include a photoionization rate for H and He as we discuss below. The time advanced ionization states for all the ions considered are found using a simple tridiagonal matrix inversion of the ionization equations for each element, using explicit, first order time differencing, with the exception of H and He for which the ionization equations can be solved in a simple closed form (given constant rates). The solution to the explicit finite difference equations becomes unreliable if the timestep is larger than  $\Delta t \gtrsim \min(1/(\alpha + \beta))$ , where  $\alpha$  and  $\beta$  are the recombination and ionization rates respectively (including the electron density) and min indicates the minimum of the quantity for the given element. As a result we divide up the timesteps to subdivisions of the hydrodynamical timestep so as to not violate the ionization timestep constraint. This is the same method we have used previously and it has been tested and proven accurate (Slavin & Cox 1992, 1993). We update the

ionization states of the ions after the Lagrangian step and before the remap since the number of each ion in a parcel should be conserved during the Lagrangian step. The fluxes of the ions must be accounted for during the remap and we take care to ensure that the sum of the ion fractions is one before and after the remap.

Another influence on the ionization and cooling in the shock is the pre-ionization of the gas entering the shock front. Modelers of plane parallel shock fronts have dealt with this question in a variety of ways. Shull & McKee (1979) calculated the ionization created by the radiative precursor, finding self-consistent values for the ionization in the ambient medium. Self-consistent in this context means that the radiative precursor creates an ionization level that is the same as that presumed when calculating the radiation field created by the shock. Cox & Raymond (1985) took a different approach. Arguing that in most cases the upstream gas does not have time to reach ionization equilibrium, they calculated “families” of pre-ionization-dependent radiative shocks in which self-consistency was not assumed. They were primarily concerned with shock diagnostics and found that faster shocks going into a low pre-ionization medium were very similar to slower shocks going into a medium with higher pre-ionization. For our purposes, we are mainly concerned with the post-shock cooling and how it affects the dynamics and temperature in the shock. Given the computational cost in calculating the ionizing radiation field for each timestep and the fact that an assumption of ionization equilibrium in the pre-shock medium is probably not justified in most cases, we instead take the simple approach of assuming either a relatively high ionization level,  $X(\text{H}^+) = X(\text{He}^+) = 0.5$  or a fairly low ionization level  $X(\text{H}^+) = X(\text{He}^+) = 0.1$  for the ambient medium. With our non-equilibrium ionization scheme, this requires fixing a photoionization rate necessary to achieve this level of ionization which then applies everywhere and at all times during the run. We also need to fix a heating rate in the medium necessary to maintain the ambient temperature assumed,  $10^4$  K. We have found that the resulting SNR evolution is not strongly affected by the different values for the ionization level and the efficiency of grain destruction (the fraction of grain mass returned to the gas phase) as a function of shock speed is essentially the same, deviating by at most 6% (see Table 2). In the rest of this paper we assume a 50% pre-ionization in the medium unless stated otherwise.

### 2.1.2. Thermal Conduction

We also include electron thermal conduction in our code using Spitzer conductivity limited by saturation (Cowie & McKee 1977). This is done in an operator split way and using a two step predictor-corrector approach. The first step is a fully implicit half timestep using the initial temperatures to calculate the conductivities. The second step uses the temperatures from the half timestep for calculating the conductivities and then does a full timestep, this time using a Crank-Nicholson (Crank & Nicolson 1996) timestep. For both steps the time-advanced temperature is found via tridiagonal matrix inversion. This approach has proven stable and accurate. Magnetic fields severely inhibit electron thermal conduction except along the field lines. We do not include

any reduction of the conduction caused by the magnetic field, but we feel this is justified since conduction is only important in the hot gas where the field should be dynamically unimportant. Balsara et al. (2008) have examined SNR evolution with anisotropic thermal conduction and found that the anisotropy can be significant, though primarily at later times in the evolution. We assume equal electron and ion temperatures in this work.

### 2.1.3. *The Magnetic Field*

The magnetic field is included approximately via a pressure term proportional to the density. This treatment of the field only applies to the perpendicular component of the magnetic field and ignores the magnetic tension, which would require at least a 2D calculation. Carrying out the calculation in 1D has allowed us to go to very high resolution, 0.0125 pc, over a volume that extends to 75 pc and is necessary in the post-shock region of the radiative shock. In addition, we are not aware of any publicly available MHD codes that include all of the physical effects that we have included in our calculations, in particular cooling with non-equilibrium ionization. A full 3D, or at least 2D calculation using realistic magnetohydrodynamics and including the non-equilibrium ionization and associated cooling would be more accurate than our calculations if sufficient spatial resolution could be achieved. We aim to carry out such calculations in the future. For such calculations, assuming an initially uniform field, we would expect the results to have a dependence on angle relative to the magnetic poles. We would expect our results presented here to most closely match those for parcels relatively close to the magnetic equator of a remnant where the magnetic field is close to being perpendicular to the shock propagation direction. A more complex, twisted or turbulent field in the ambient medium could lead to the magnetic tension playing less of a role and to the SNR evolving in a way similar to our results over much of its area where the magnetic pressure is the dominant influence.

### 2.1.4. *Standard Run Parameters*

For our standard run we used an explosion energy of  $5 \times 10^{50}$  ergs, somewhat less than is usually considered for the initial explosion for SNRs, though we have also done a run with twice that explosion energy. Because of energy losses to cosmic rays relatively early in the lifetime of a SNR, a remnant with an initial explosion energy of  $10^{51}$  ergs may resemble one with a lower explosion energy that did not have cosmic ray losses. In addition the explosion energy derived for some older remnants, such as the Cygnus Loop, is below  $10^{51}$  ergs. The density and magnetic field for our standard run were  $0.25 \text{ cm}^{-3}$  and  $3 \text{ } \mu\text{G}$  and the ambient temperature was assumed to be  $10^4 \text{ K}$ . We consider these values to be fairly representative of the warm ISM and they match the values for steady shocks used by JTH96, which allows for simpler comparisons to their results. We have also done runs with higher ambient density and lower magnetic field strength. We discuss the effects of these parameters on the amount of grain destruction in §3.3.

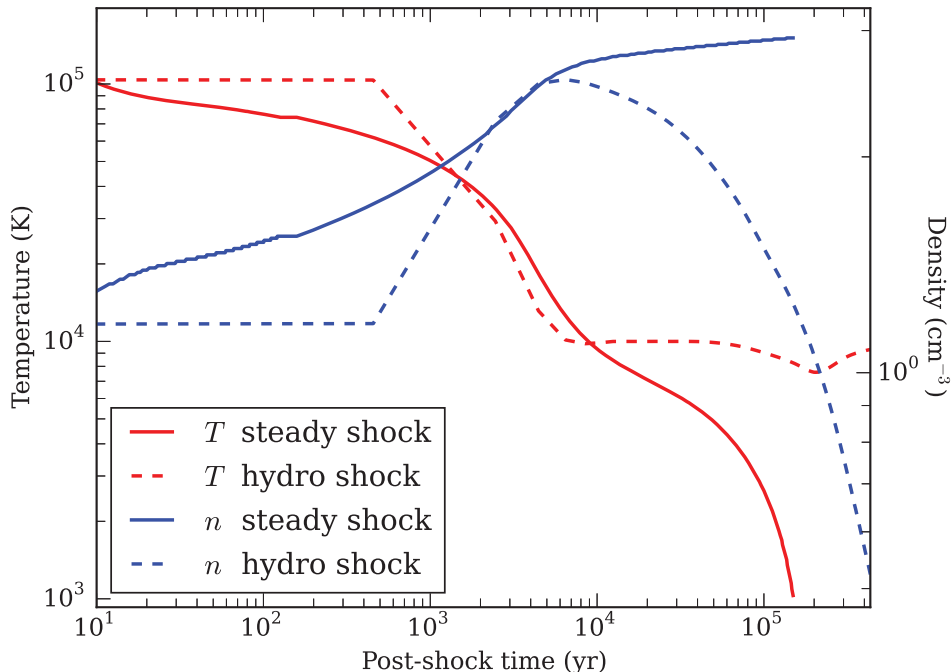


Fig. 1.— Comparison of  $100 \text{ km s}^{-1}$  shock profiles for the steady, plane parallel shock used by JTH96 and the effective profile we calculated for our standard hydrodynamical evolution. Note the dropoff of the density for the hydrodynamical case. This is caused by the spherical divergence for the radially expanding shock. The flattening of the hydro shock temperature profile at  $T \sim 9000 \text{ K}$  is caused by the switching off of cooling below  $10^4 \text{ K}$ .

## 2.2. Parcel Trajectories

After carrying out the hydrodynamical runs we have created parcel “trajectories”, i.e. histories of the temperature, density and ionization of individual parcels. Using these, in addition to the shock speed as a function of time, allowed us to create shock profiles for parcels that begin when the shock overruns them, at a given radius. This is made considerably easier by the fact that the calculations are 1D, so the mass coordinate,  $m(r) \equiv \int_0^r \rho(r') 4\pi r'^2 dr'$ , for a given radius identifies the location of a parcel. The effective shock profiles can be compared with those generated by steady, plane parallel shock calculations and can be used to calculate grain destruction as the parcel moves through the shock. In Figure 1 we compare the steady shock profile for a  $100 \text{ km s}^{-1}$  shock used in JTH96 with the profile we generated for a parcel shocked to  $100 \text{ km s}^{-1}$  in our standard case hydrodynamical evolution. The steady shock profile is done at much higher spatial resolution than our hydro calculations, but a fairly close match is seen. The most striking difference between the profiles is in the density, which drops off in the post-shock region for the hydro calculation because of the spherical divergence. The post-shock temperature in the hydro calculation stops dropping

and flattens out at  $\sim 9000$  K because, as described above, we turn off cooling and turn on heating for  $T < 10^4$ . As we show below, the grain destruction for these profiles turns out to be nearly the same.

### 2.3. Grain Processing

Grain processing in shocks occurs because of the acceleration of the grains and the compression and heating of the gas. Both gas-grain interactions (primarily sputtering) and grain-grain collisions are important in grain destruction and erosion. The grain processing codes that we use are nearly the same as those used by JTH96, though we have revised the dust charging scheme as described below. The code reads in the shock profile and integrates through it calculating the grain processing. The processes included are thermal sputtering, i.e. sputtering caused by thermal ions, non-thermal (a.k.a. inertial) sputtering caused by the relative speed of the grains and the gas, and shattering and vaporization caused by grain-grain collisions. We note that thermal and inertial sputtering can be combined, using a skewed Maxwellian distribution as in Draine & Salpeter (1979b) and Bocchio et al. (2014, hereafter BJS14), though we have not done that in this work. The differences between the two approaches is most pronounced for case in which the thermal velocity of the gas and drift velocities of the grains are similar. The sputtering rates we use are the same as in JTH96. BJS14 have used updated rates for carbonaceous grains based on the work of Serra Díaz-Cano & Jones (2008), with the assumption that the carbonaceous grains are hydrogenated amorphous carbon (a-C:H). We use the older rates that apply to graphitic grains in this work. The assumption that the carbonaceous grains are a-C:H type leads to more destruction as we discuss below.

Because shattering re-distributes grain mass into smaller grains, mass bins must be followed (see JTH96 for details). For most of the calculations, we divide the grain mass into five bins initially, with an extra bin on the low end to contain small grains that result from shattering or sputtering. JTH96 found that there was little difference in the grain destruction results if a larger number of bins were used. We have found this to be the case for our calculations as well. However, to make the visualization of the redistribution of grain mass caused by shattering clearer, we have also carried out calculations using an initial seventeen mass bins with seven initially empty small mass bins for our standard run.

#### 2.3.1. Grain Parameters

The grain parameters that we adopt are the same as those used by JTH96 so as to facilitate comparison with their results. We use two grain types, silicates and carbonaceous grains with assumed solid material densities of  $3.3$  and  $2.2 \text{ g cm}^{-3}$  respectively. We assume an initial Mathis et al. (1977, hereafter MRN) type power law size distribution ( $dn/da \propto a^{-3.5}$ ) for both the carbonaceous



and silicate grains. The smallest and largest grain sizes at the start of the grain evolution calculations are 0.005 and 0.25  $\mu\text{m}$  for both grain types used. The assumed gas-to-dust mass ratio in the ambient medium (including He in the gas mass) is 163. The included dust destruction processes, i.e. thermal sputtering, non-thermal sputtering, shattering and vaporization, involve a number of physical parameters and we refer the reader to JTH96 for a detailed discussion of them. Here we just note that the assumed atomic mass for silicate grains is 5.7 u and 4 u for the carbonaceous grains and the threshold velocity for shattering is 2.7 km s<sup>-1</sup> and 1.2 km s<sup>-1</sup> for silicate and carbonaceous grains respectively. Much of the destruction in radiative shocks begins with shattering, which creates small grains which are then sputtered, though also slowed more quickly than larger grains.

We acknowledge that this model for the size distribution and grain composition is not consistent with all of the observational constraints. More recent models (Weingartner & Draine 2001; Zubko et al. 2004; Jones et al. 2013; Siebenmorgen et al. 2014) have been constructed that are better able to fit the various observational constraints on the dust such as the infrared emission and abundance constraints as well as the extinction curve. Those models use more complicated grain size distributions and more realistic grain compositions. In the future we aim to test the effects of these grain models on grain destruction timescales, but in this work our primary aim has been to compare with the steady state plane parallel shock calculations that have been carried out previously and therefore we have used the same grain model as in JTH96.

### 2.3.2. Grain Charge

The interaction of dust with the plasma depends in various ways on its charge. JTH96 used the rough analytical fit of McKee et al. (1987) to the results of charging calculations to determine the dependence of grain charge on the gas temperature, relative gas-grain speed and UV radiation field. We have updated the grain charge calculations using the scheme from Weingartner & Draine (2001) with updates from Weingartner et al. (2006) and modifications to include the relative gas-grain velocity, which alters the charging rates for electron and ion grain collisions. In this work we adopt the standard tight coupling approximation, in which it is assumed that the gas and grains remain coupled throughout the shock. Under these conditions, the value of the grain charge has only a limited role. The grain undergoes betatron acceleration when the magnetic field increases because of compression, but though this is mediated by the grain charge, the actual value of the charge does not come into the calculation of the grain speed. The only effect of the charge in this scheme is in its effect on the plasma drag on the grains and the small Coulombic modification to the cross section for sputtering. We note that the grain charge can be much more important if the gas and dust decouple as can occur for larger grains (see Slavin et al. 2004).

An input that is needed for the grain charging calculations is the yield-averaged UV flux.



Following McKee et al. (1987) we define

$$G_0 = \frac{\int_{8\text{eV}}^{\infty} d\nu Y(h\nu) 4\pi J_\nu / h\nu}{2.4 \times 10^6 \text{ cm}^{-2} \text{ s}^{-1}}, \quad (1)$$

where  $Y$  is the photoelectric yield and  $J_\nu$  is the mean intensity of the radiation field and  $2.4 \times 10^6 \text{ cm}^{-2} \text{ s}^{-1}$  is the “average” yield averaged UV field as adopted by Draine & Salpeter (1979a). In principle, given the temperature, density and ionization at every point in the remnant as a function of time, one could calculate this quantity at each radius and time. However, in detail it becomes more complex since the largest contributors to  $J_\nu$  are resonance lines, in particular H Lyman  $\alpha$ , that have substantial optical depth in the shock region. Thus scattering is important and an accurate calculation would require a radiative transfer calculation for each location and time. Given the limited role of grain charge for the grain destruction calculations, we take a simpler approach. Following McKee et al. (1987) we take  $4\pi J(\text{Ly}\alpha) = 30F(\text{Ly}\alpha)$ , where  $F(\text{Ly}\alpha)$ , is one half the integrated column emissivity of H Lyman  $\alpha$  in the shock and  $J(\text{Ly}\alpha)$  is the mean intensity. The factor of 30 here comes from both geometrical effects (effective extent of the front perpendicular to the shock, a factor of  $\sim 3$ ) and enhancement caused by scattering (a factor of  $\sim 10$ ). In addition we assume that there is a diffuse background equal to the Draine & Salpeter (1979a) field. Doing this we find for our standard run that  $G_0$  has a peak of  $\sim 2.7$  for shock speeds near  $115 \text{ km s}^{-1}$  falling off sharply at higher velocities and more gradually toward lower speeds, reaching 1.4 at  $v_{\text{shock}} = 40 \text{ km s}^{-1}$ , which is the shock speed at the end of the standard run. These values are somewhat higher than those reported by McKee et al. (1987), though that could be caused, especially for the slower shocks, by the effects of earlier shocks that affect the post-shock gas that was shocked to a higher speed. The effects of the radiation field on the grain destruction is minor, since in tests we have done, an increase by a factor of ten on  $G_0$  did not change the overall grain destruction efficiency substantially.

### 3. Results

#### 3.1. SNR Evolution

To assess the impact of SNR shocks on dust destruction one needs to follow SNR evolution well beyond the point at which the remnant becomes radiative. This is because not only do the relatively slow shocks of late stage remnants still destroy dust, they also sweep up increasing volumes of the ISM such that even with a low efficiency of grain destruction, slow shocks are important for the overall grain destruction in the ISM. In addition, for our calculations we need to follow the gas parcels that have been shocked for a long enough time that the grain destruction rate has become negligible. For our standard run we follow the evolution until the shock speed drops to  $41 \text{ km s}^{-1}$  at a radius of 62 pc,  $5.4 \times 10^5 \text{ yr}$  after the explosion. The magnetosonic speed in the ambient medium is  $17.2 \text{ km s}^{-1}$ , so it is a mach 2.4 shock with a post-shock maximum compression of 3.9 (after cooling). We note that this compression factor is less than estimated by McKee et al. (1987)

for a magnetically supported post-shock, compression region,  $\chi_{\max} = 0.767 v_{\text{shock}} n_a^{1/2} / B_a$ , where  $\chi$  is the compression factor,  $v_{\text{shock}}$  is the shock speed in  $\text{km s}^{-1}$ ,  $n_a$  is the ambient density in  $\text{cm}^{-3}$  and  $B_a$  is the ambient magnetic field in  $\mu\text{G}$ . That expression yields a value of 5.24 for this shock. We find that in general the maximum post-shock compression in our hydrodynamical calculations is below that predicted by McKee et al.’s expression since thermal pressure also contributes to the post-shock pressure and the spherical divergence and expansion over time causes the pressure to decline behind the shock.

Figure 2 shows the shock radius and shock speed evolution over time for our standard run. The precipitous drop in shock speed at just below  $200 \text{ km s}^{-1}$  is clearly visible and indicated on the plot. As shown the shock is briefly re-accelerated when the previously shocked material catches up with the slowing cold shell. This leads to greater compression at this time and cooling of the hot shocked gas just inside of the cooled radiative shell as it runs into and is compressed against the shell. This is illustrated in Figure 3 which shows the evolution of gas parcels.

Figure 3 and Figure 4 illustrate how gas parcels shocked to a range of shock speeds evolve within the remnant. The parcels highlighted in the figures are at initial radii ranging from 24.075 pc to 39.075 pc and are shocked to speeds ranging from 86 to  $285 \text{ km s}^{-1}$ . The first time shown,  $6 \times 10^4 \text{ yr}$  after the explosion, is at a point when the remnant is just beginning to go radiative, as can be seen in Figure 3 from the density profile, which has a peak value a little greater than 4 times the ambient density of  $0.25 \text{ cm}^{-3}$ . By following the different parcels over time one can see that the density and temperature evolution is complicated for some parcels. This can be seen clearly in Figure 4 which shows the time evolution of the same parcels. In particular, the parcel marked by circles (first parcel to be shocked) can be seen to be compressed and heated, then expand (density decreases) and finally get recompressed and cooled because of catching up with the cold shell.

There have been many numerical calculations of SNR evolution carried out over the years (e.g., Cox 1972; Chevalier 1974; Cioffi et al. 1988; Slavin & Cox 1992). Cioffi et al. (1988) analyzed the results of their 1D (spherically symmetric) numerical calculation of radiative remnant evolution, which did not include any magnetic pressure, and found that the late time shock radius evolution could be well described by an offset power-law,  $R_s = R_{\text{PDS}}(4/3t_* - 1/3)^{3/10}$ , where  $R_{\text{PDS}}$  and  $t_*$  are functions of the explosion energy, ambient density and metallicity. We find that we can also fit the late time shock radius evolution with such an offset power law, but with a somewhat different exponent. For our standard case we find the late time behavior is not well fit by the Cioffi et al. (1988) formula and instead fit a general offset power law,  $R_s \propto (t - t_{\text{off}})^\gamma$  to the expansion. This yields  $R_s = 0.494(t + 1.79 \times 10^4 \text{ yr})^{0.365} \text{ pc}$ . Note in particular that we get an offset time with the opposite sign from that in the Cioffi et al. formula. In general we expect that including magnetic pressure will lead to faster expansion since the total pressure in the shell is dominated by magnetic pressure. The late time expansion is thus maintained primarily by the energy stored in the magnetic field of the shell rather than the thermal energy in the hot bubble. Since the overall grain destruction rate depends on the mass of gas shocked to a given speed,  $M(v_s)$ , the shock speed as a function of radial distance from the explosion center is important. We discuss this further below.

Table 1. Comparison of Modeled Grain Destruction Efficiencies (%)

Ref. <sup>a</sup>	$v_{\text{shock}}$ (km s <sup>-1</sup> )						
	50	75	100	125	150	175	200
Carbonaceous grains							
JTH96	1	5	7	13	12	21	47
BJS14	77	83	91	96	99	100	100
this study	1	4	10	18	17	18	23
Silicate grains							
JTH96	2	12	18	33	32	41	49
BJS14	2	12	29	46	53	67	67
this study	2	9	23	40	41	42	40

<sup>a</sup>The references correspond to: JTH96, Jones et al. (1996), and BJS14, Bocchio et al. (2014). “this study” refers to our standard run that uses the parameters in the first line of Table 2. Note that the results for the 75, 125 and 175 km s<sup>-1</sup> shock speeds were not presented in JTH96 but were calculated using the same code later.

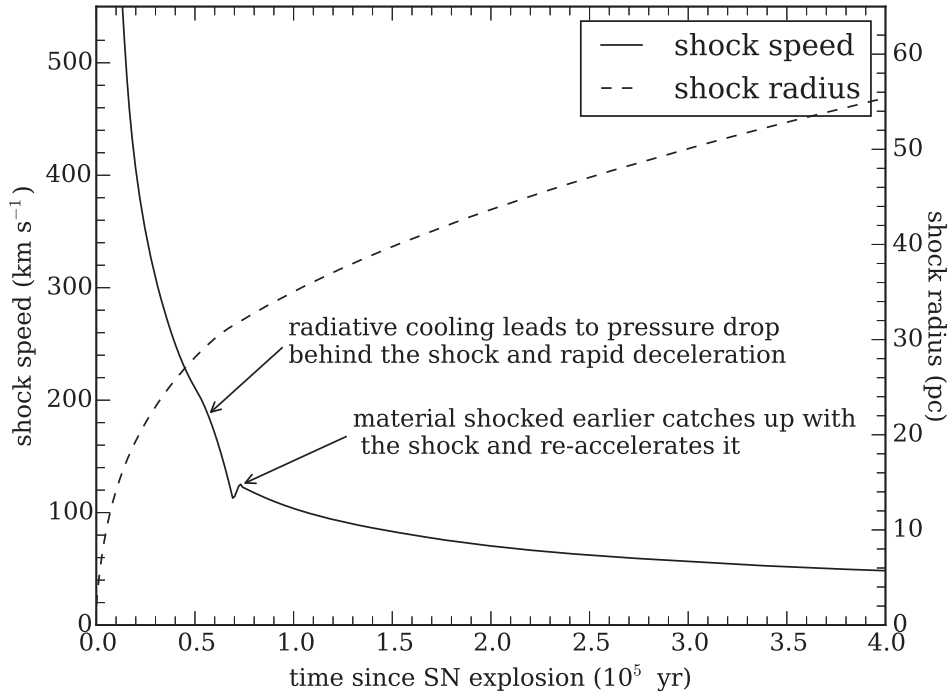


Fig. 2.— Shock radius and shock velocity evolution for our standard, supernova remnant run ( $E_0 = 0.5 \times 10^{51}$  ergs,  $n_a = 0.25 \text{ cm}^{-3}$ ,  $B_a = 3 \mu\text{G}$ ). Once the remnant begins to go radiative at  $t \approx 5 \times 10^4$  yr, the shock speed drops sharply and then rebounds after previously shocked material catches up with the decelerating shock. As a result of the sharp drop in shock speed there is a range of speeds,  $v_{\text{shock}} \approx 120 - 190 \text{ km s}^{-1}$ , that exists for only a short time and in a small volume of the ISM.

### 3.2. Grain Destruction Efficiency

The grain destruction efficiency is defined as the fraction of the mass originally contained in grains that is returned to the gas phase either through sputtering or vaporization of the grains. Grains that are fragmented are not considered to be destroyed. Their mass is distributed into lower mass bins (see JTH96 for a more thorough discussion and Figure 6). In Figure 5 and 6 we illustrate the destruction and re-distribution of grain mass for shocks of a range of speeds for our standard run. In Figure 5 we plot, instead of the destruction efficiency, the ratio of final mass over initial mass in each bin,  $m_{kf}/m_{ki}$  where  $m_{ki}$  is the initial mass contained in bin  $k$  and  $m_{kf}$  is the final mass contained in the bin. Mass is lost to a bin in one of three ways: 1) via sputtering (in which case the sputtered mass fraction is lost to the dust phase), which causes grains to move down to lower mass bins, 2) vaporization, which causes the entire grain mass to be lost to the dust phase or 3) shattering, in which case no mass is lost to the dust phase, but the mass is redistributed to the lower mass bins. Altogether these processes tend to cause a substantial loss of large grain

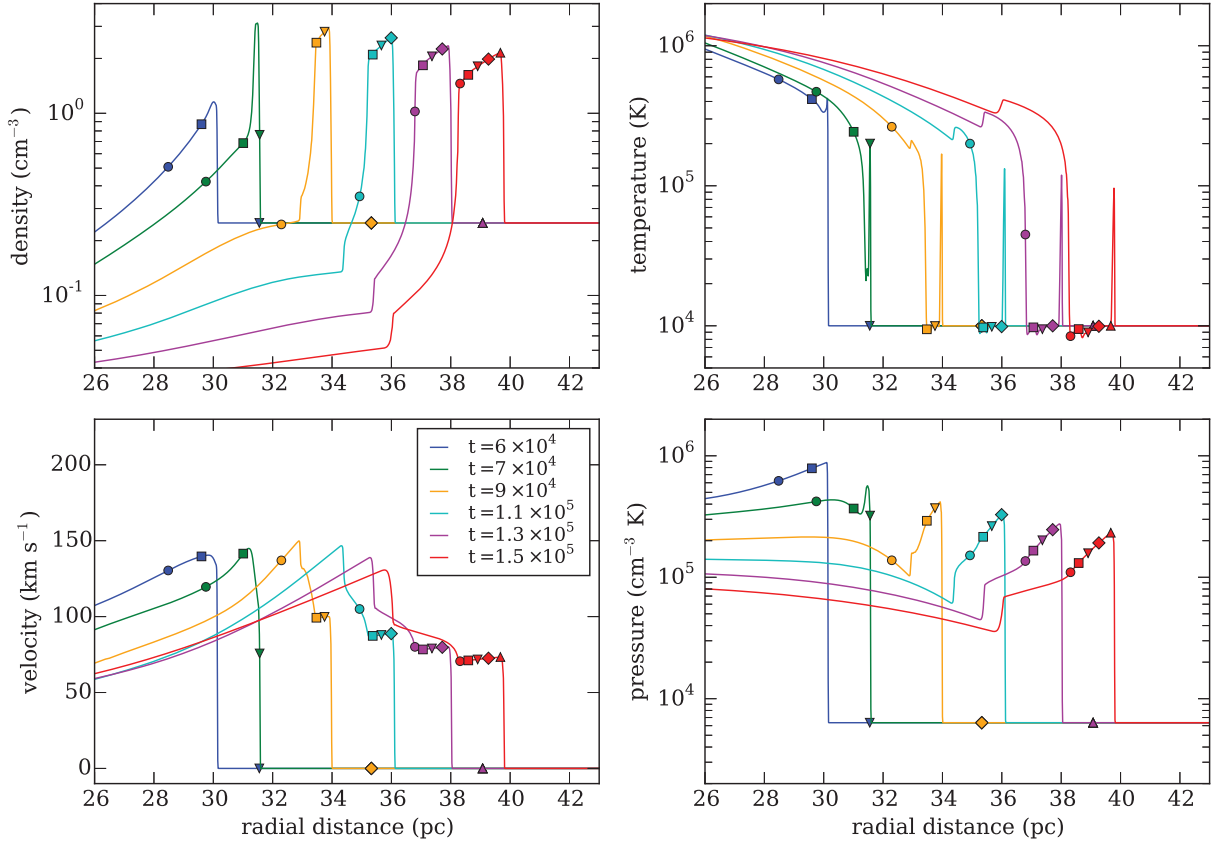


Fig. 3.— Evolution of individual gas parcels within our standard SNR evolution run. Gas parcels are identified by their marker shape, while the colors correspond to time snapshots. The initial radii of the parcels are 24.075, 27.825, 31.550, 35.325 and 39.075 pc from the center of the SNR. The corresponding speeds to which these parcels were initially shocked are: 285, 215, 114, 102, and 86 km s<sup>-1</sup>, respectively. See text for more discussion. Note that the pressures shown in the lower right panel are the total pressures including thermal and magnetic pressures.

mass, mostly from shattering, with the mass in small grains increasing relative to the initial size distribution. These results are illustrated in Figure 5 where, in the upper plots, the white line divides the area in which mass is removed from the mass bins from that in which there is a net gain of mass. Because of the non-monotonic shock speed evolution, we cannot show the results on these plots for all the shocks with speeds  $\sim 125$  km s<sup>-1</sup> and we simply choose the first time a shock speed was encountered for display purposes. Since in the plots in Figure 5 we are plotting the ratio relative to the initial mass, we cannot include bins that are initially empty. For that reason we also plot the absolute mass distributions in Figure 6. More specifically we plot  $m \, dn/d(\ln m) = ma/3 \, dn/da$ , where  $m$  is the grain mass and  $dn/da$  is the size distribution initially  $\propto a^{-3.5}$  (MRN distribution).

We show in Figure 7 our calculated destruction efficiency vs. shock speed with a comparison

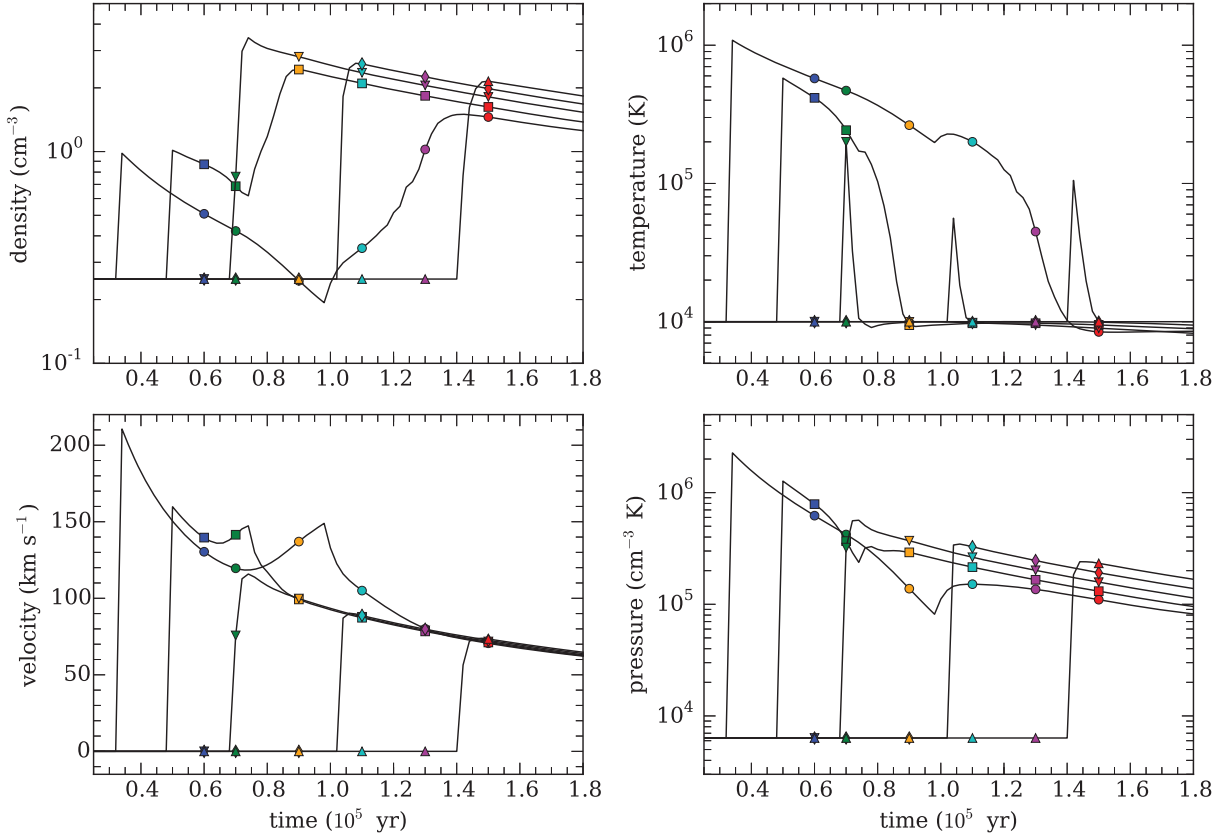


Fig. 4.— Evolution of individual gas parcels with time. Here we show the time evolution of the fluid variables for the same parcels as shown in Figure 3 with the same marker symbols. The color of the symbol corresponds with the time as in Figure 3. These are the shock profiles that are input into the grain evolution code that calculates grain processing including destruction via sputtering and vaporization and shattering (though the time used for each profile is relative to when the parcel is first shocked). Note in particular the non-monotonic evolution of the density and temperature for the parcel represented by a circle. The blastwave velocity was  $285 \text{ km s}^{-1}$  when this parcel was shocked and it was heated to  $1.1 \times 10^6 \text{ K}$ . Even many parcels that were shocked to high temperatures initially, cool well before their initial post-shock radiative cooling times would predict because of being compressed against the dense shell.

to the results for steady plane-parallel shocks as in JTH96. In Table 1 we compare our results with those of JTH96 and BJS14. The large differences between the efficiency of carbonaceous grain destruction found by BJS14 and both JTH96 and this study derive from the different grain model used by that work. Rather than the graphite-like carbonaceous grains used by JTH96, BJS14 use hydrogenated amorphous carbon (a-C:H) as their model for carbonaceous grains and employ the sputtering yield results of Serra Díaz-Cano & Jones (2008). The sputtering yield for this type of

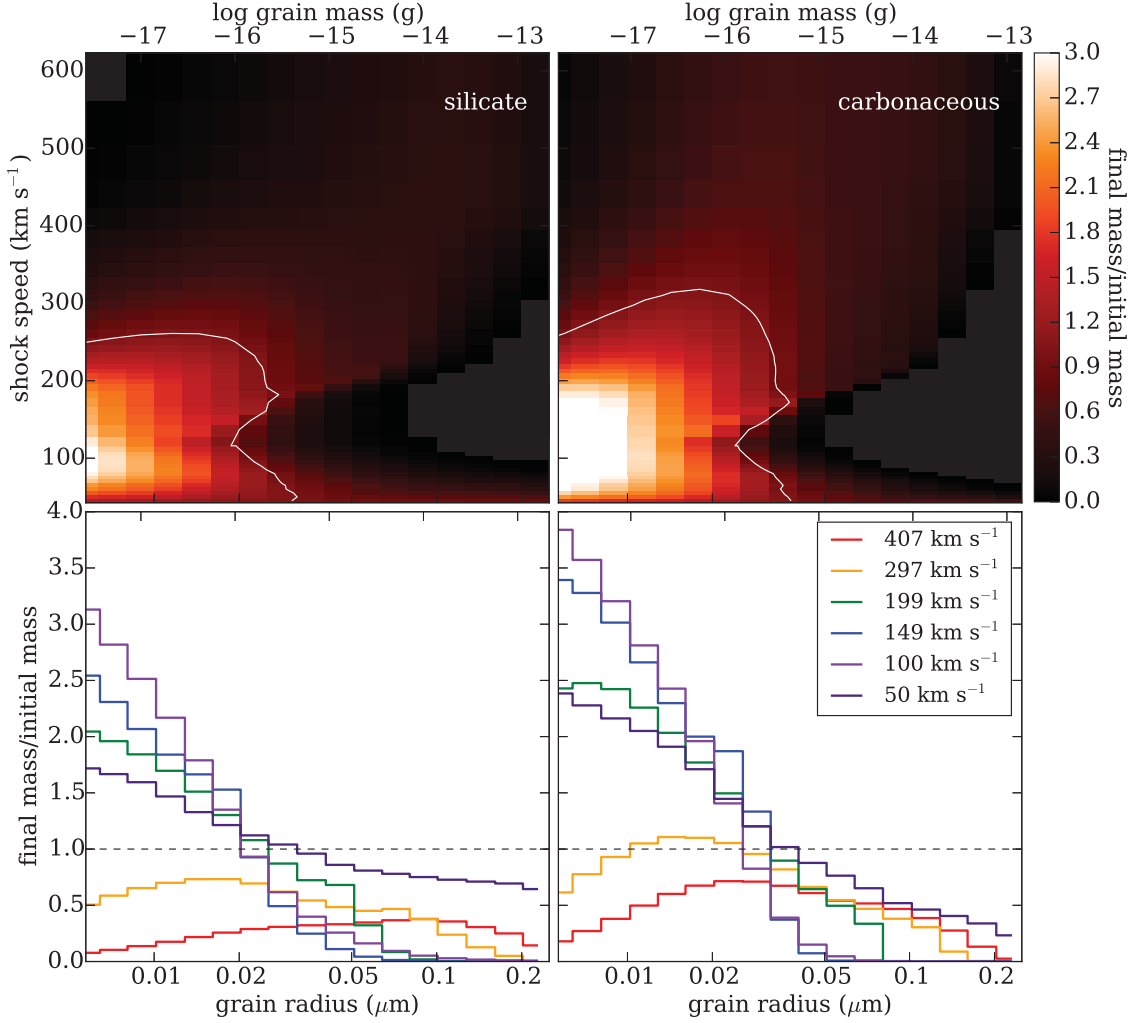


Fig. 5.— Ratio of final grain mass/initial grain mass in size/mass bins as a function of shock speed and grain size (top) for silicate grains (left) and carbonaceous grains (right). The bottom plots show the same data as line plots of mass ratio as a function of size/mass bin for selected shock speeds. The white contours in the top plots show the division between bins for which there is a net gain in mass and those for which there is a net loss. The dashed line in the bottom plot shows the same division between net increase and decrease of mass in a size bin. The size bins are logarithmically spaced in mass. Although it may appear that there is an overall increase in mass for some shocks, the increase in each bin is relative to the initial value and since most of the mass is in the large size/high mass bins initially, so in fact dust mass is lost in all cases. These results are for our standard run.



carbonaceous grain is substantially greater than that for graphite due to a lower binding energy and density for a-C:H. In addition, BJS14 use different size distributions for both the carbonaceous and silicate grains. Since grain-grain collisions are important for altering the grain size distribution in shocks, a different initial size distribution can have a substantial impact on the grain processing. Finally, BJS14 include mantles on the silicate grains entering the shock. These are features of the Jones et al. (2013) dust model, which differs significantly from the MRN model used by JTH96 and by us in this work.

We have recalculated the steady shock efficiencies using a slightly modified version of the GRASH code employed by JTH96, using updated grain charge calculations as discussed above. We have also supplemented the original four steady shock speeds (50, 100, 150 and 200 km s<sup>-1</sup>) with three additional shock speeds (75, 125, and 175 km s<sup>-1</sup>) using shock profiles kindly provided to us by John Raymond. As we have noted, for an evolving SNR that goes radiative, shock speed does not evolve monotonically because of the sudden drop in post-shock pressure and shock speed and subsequent re-acceleration that occurs at  $v_s \sim 125$  km s<sup>-1</sup>. This is why the efficiency vs.  $v_s$  curves are multivalued in the figure. As can be seen in the figure, the hydrodynamical calculations agree with the steady, plane parallel shock results quite closely for most of the range covered by the steady shock calculations. The exception is at the high shock speed end. The difference for these shocks seems to be caused by the non-steady hydro evolution when the radiative losses are just starting to become important. For this period, the shocked gas does not radiate immediately but cools slowly

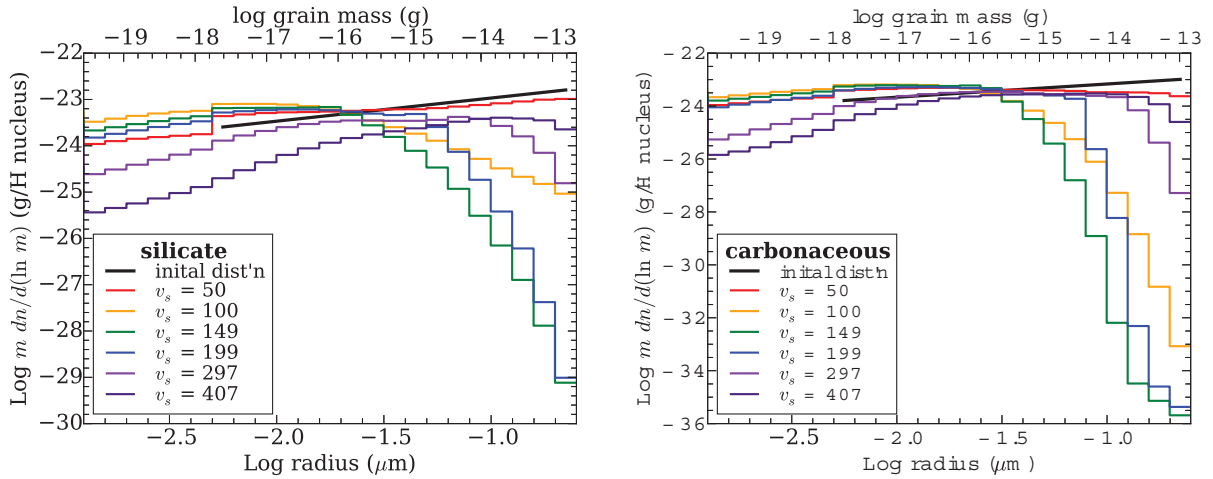


Fig. 6.— Grain mass distribution vs. grain size and mass for several different shock speeds for our standard hydro run. This version of the size distribution illustrates that most of the mass is at the high mass end of the size distribution and is proportional to  $a^4 dn/da$ , where  $dn/da$  is the standard size distribution. Note that the initial MRN-type size distribution extends only from  $0.005 \mu\text{m}$  to  $0.25 \mu\text{m}$ , but after shock processing much of the grain mass gets shifted to smaller (lower mass) grains primarily because of shattering.

at first, only forming a cold shell after  $\sim 10^4$  yr. In the hydro case, compression is initiated by the shocked gas catching up to the slowing shell, because later, slower shocks go radiative much more quickly. Thus for the shocks with speeds near  $200 \text{ km s}^{-1}$ , the gas is first compressed and only then cools because of the higher density. The compression causes an increase in magnetic pressure that causes a back reaction that causes the shell to re-expand somewhat before it has fully cooled. This prevents the post-shock gas from reaching the high densities that it does for steady shock evolution and therefore the grains do not get as much acceleration with accompanying destruction.

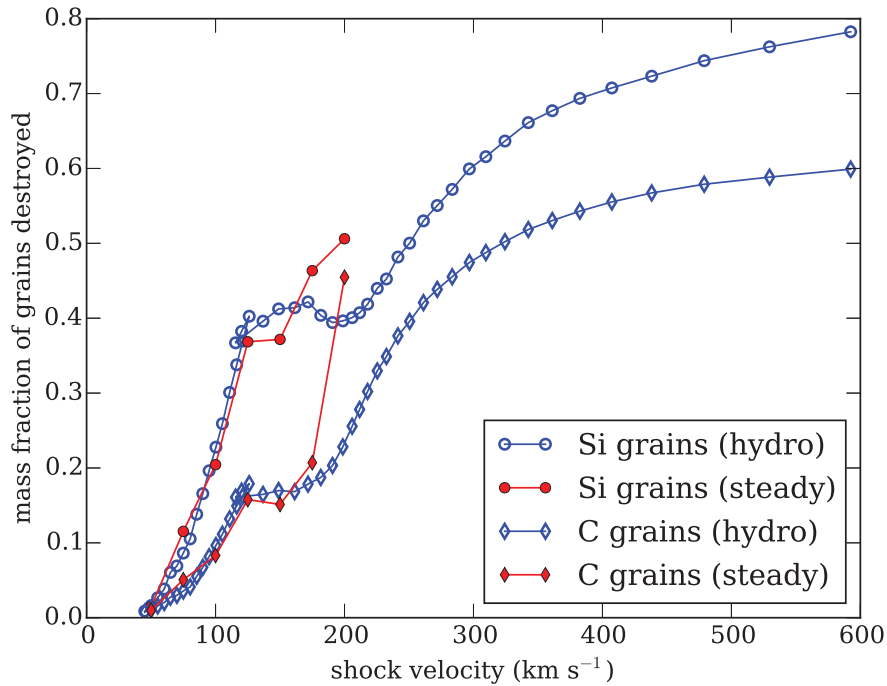


Fig. 7.— Grain destruction efficiency vs. shock velocity for our standard hydrodynamical run compared to that for steady, plane parallel shocks. The results for our hydro runs are clearly quite close to those for the steady shocks except for near  $v_s \approx 200 \text{ km s}^{-1}$  where the hydro runs yield a substantially smaller efficiency. The cause of this lower efficiency is the early onset of compression because of running into the rapidly slowing shock in the hydrodynamical evolution. The magnetic field causes a partial re-bounce before cooling sets in followed again by expansion because of spherical divergence. These effects lead to less compression and therefore less grain acceleration and destruction in the shock.

To understand the efficiency of dust destruction in the ISM we must use the efficiency for the evolving SNR shocks in conjunction with information on the expansion of the SNR. The mass of gas in which the dust has been destroyed can be calculated by (e.g., Dwek & Scalo 1980)

$$M_g = \int \epsilon(M_s) dM_s, \quad (2)$$

Table 2. Mass of Gas with Cleared of Dust for SNR Models<sup>a</sup>

$E_{51}$	$n_a$ (cm <sup>-3</sup> )	$B_a$ (μG)	$X_H$ <sup>b</sup>	TC <sup>c</sup>	$M_{Si}$ (M <sub>⊙</sub> )	$M_C$ (M <sub>⊙</sub> )
0.5	0.25	3.0	0.5	on	990	600
0.5	0.25	3.0	0.1	on	980	600
0.5	0.25	3.0	0.5	off	960	580
1.0	0.25	3.0	0.5	on	1990	1220
0.5	0.25	0.3	0.5	on	1490	780
0.5	1.00	3.0	0.5	on	1020	640
Steady shock/HIM dominated <sup>d</sup>						
1.0	0.25	3.0	...	...	1700	990

<sup>a</sup>The masses are the efficiency of dust destruction (fraction of grain mass destroyed) integrated over gas mass enclosed by the shock over the calculated SNR evolution (see Eq. 2 and text). The first line in the table corresponds to our standard case.

<sup>b</sup>Hydrogen ionization fraction in the ambient medium. Helium is assumed to have the same ionization fraction.

<sup>c</sup>Thermal conduction — either turned on or off.

<sup>d</sup>These values are for the hot gas dominated ISM model as discussed in JTH96 and in the text (§§4.2 and 4.3) and include a factor of  $f_c/f_h = 0.3/0.7$  (the ratio of warm cloud to hot gas filling factors; values without this factor are 4000 and 2300 M<sub>⊙</sub> for silicate and carbonaceous grains respectively). We used a somewhat different interpolation/extrapolation of the grain destruction efficiency than JTH96 to derive these results (see text).

where  $\epsilon$  is the grain destruction efficiency and  $M_s$  is the mass of shocked gas. This has been sometimes been converted to an integral over  $v_s$ ,  $\int \epsilon(v_s) dM_s/dv_s dv_s$ , but this cannot be done easily when  $v_s$  is not monotonic with  $M_s$  as is our case. This integral gets cut off at the low (mass) end by the small amount of gas that is shocked to high velocities and at the high end by the low grain destruction efficiency at low shock velocities, which goes to zero as  $v_s$  approaches the signal speed of the ambient medium. We list the mass of gas cleared of dust in Table 2. We did not find a simple fitting formula for  $\epsilon$  for our standard hydro run, but it can be approximated by

$$\epsilon(v_{s7}) = \begin{cases} 0.05 - 0.19 v_{s7} + 0.215 v_{s7}^2 + 0.0200 v_{s7}^3 & 0.4 < v_{s7} < 1.25 \\ 0.175 & 1.25 \leq v_{s7} < 1.85 \\ -1.9 + 2.02 v_{s7} - 0.641 v_{s7}^2 + 0.0922 v_{s7}^3 - 0.00498 v_{s7}^4 & 1.85 \leq v_{s7} < 5 \end{cases} \quad (3)$$

where  $v_{s7} = v_s/100 \text{ km s}^{-1}$ .

In addition to our results for our hydrodynamical calculations, we present in Table 2 results for steady shock calculations as in JTH96. For those models, the assumed pre-shock ionization depended on the shock speed and so is not listed in the table. JTH96 provided an approximate fit to their destruction efficiency results that included an extrapolation to  $300 \text{ km s}^{-1}$ . The fit was based on results only for 50, 100, 150 and  $200 \text{ km s}^{-1}$  shocks. We have used our calculated steady shock values at 75, 125, and  $175 \text{ km s}^{-1}$  to get a more accurate interpolation and have used an almost flat extrapolation to  $500 \text{ km s}^{-1}$  rather than their sharply rising extrapolation. The newly calculated interpolation and values tend to lie above the old fit, especially near  $125 \text{ km s}^{-1}$ , which contributes significantly to the integral for  $M_g$ . Our extrapolation for shock speeds above  $200 \text{ km s}^{-1}$  is probably a lower limit, though at those high shock speeds the contribution to the integral is not very large. As noted in footnote d of the table we include the factor of  $f_c/f_h = 0.3/0.7$ , the ratio of warm cloud to hot gas filling factors, in the mass calculated for the steady shocks. The reasoning behind this and the importance of the ISM model for grain destruction estimates is discussed in §4.2. Also mentioned in the footnote is that the values without this factor are roughly 4000 and  $2300 M_\odot$  for silicate and carbon grains respectively. These values are roughly 10 - 15% higher than the JTH96 results.

### 3.3. Effects of Parameter Choices

In order to assess the effects of the various assumptions that we have made for our standard run, we have done a series of hydrodynamical runs with different parameters. Besides our standard run, which corresponds to the first line in Table 2, we tested the effects of changing the pre-ionization in the ambient medium ( $X_H$ ), turning off thermal conduction in the hot gas, higher explosion energy ( $E_{51} = 1$ ), lower magnetic field ( $B_a = 0.3 \mu\text{G}$ ), and higher ambient density ( $n_a = 1.0 \text{ cm}^{-3}$ ). We find that neither changing the pre-ionization nor turning off thermal conduction have significant effects on the destroyed dust mass. Doubling the explosion energy approximately doubles the amount of dust mass destroyed. This is to be expected since the mass shocked to a given velocity

is directly proportional to the explosion energy in the adiabatic (Sedov-Taylor) case. For radiative remnants this scaling is not guaranteed, but Cioffi et al. (1988) find this scaling to be approximately true for their radiative remnant calculations and we also find that that scaling is roughly obeyed. There is also a strong effect of decreasing the magnetic field. Since the shell is supported by the field after the shock goes radiative, the amount compression goes roughly inversely with  $B_a$ . Thus the lower field leads to higher compression, more grain acceleration and more grain destruction. In our results, the increase is about 50% and 30% for silicates and carbonaceous grains respectively. Finally, the increase in density also increases the grain destruction level, though the effect is not nearly as strong as that of decreasing the magnetic field strength. The increased density causes the remnant to go radiative at an earlier time and for shocks that are slower. The larger cooling rate and accompanying higher compression caused by the higher density causes more grain acceleration, however this effect is counteracted to some extent by greater drag on the grains caused by the higher density. For the case that we have explored the increase in gas mass cleared of dust is only 3% and 7% for silicate and carbonaceous grains respectively. These results are consistent with those of JTH96 for shocks into a higher density ambient medium.

#### 4. Discussion

Our ultimate goal in this work is to understand the evolution of dust in the ISM. To make progress in this project we need a way to apply our calculations of grain processing in individual SNRs to the ISM as a whole. Dwek & Scalo (1980) considered these questions and found the following relation for the dust destruction timescale:

$$\tau_{\text{dust}} = \frac{\tau_{\text{SN}} M_{\text{ISM}}}{M_g} = \frac{\Sigma_{\text{ISM}}}{\mathcal{R}_{\text{SN}} M_g} \quad (4)$$

where  $\tau_{\text{SN}}$  is the mean interval between supernovae in the Galaxy (the inverse of the rate),  $M_{\text{ISM}}$  is the total mass in dust and gas in the Galaxy,  $M_g$  is the mass of gas that is cleared of dust per SN from Eq. 2,  $\Sigma_{\text{ISM}}$  is the surface density of gas and dust in the ISM and  $\mathcal{R}_{\text{SN}}$  is the supernova rate per unit area. Thus the destruction timescale can be defined in a global way in the ISM as a whole using  $\tau_{\text{SN}}$  and  $M_{\text{ISM}}$  or locally in some suitably large region of the ISM using  $\Sigma_{\text{ISM}}$  and  $\mathcal{R}_{\text{SN}}$ . Since the dust destruction timescale depends on these combinations of quantities, we will refer to either  $\tau_{\text{SN}} M_{\text{ISM}}$  or  $\Sigma_{\text{ISM}}/\mathcal{R}_{\text{SN}}$  as the SN mass interval and denote it by  $\mathcal{N}$ .

##### 4.1. SN mass interval

It is clear that the SN mass interval is a critical factor in assessing the effectiveness of grain destruction though it depends on two uncertain quantities. JTH96 and Bocchio et al. (2014) used the global values from McKee (1989),  $\tau_{\text{SN}} = 125$  yr and  $M_{\text{ISM}} = 4.5 \times 10^9 M_{\odot}$ , for a value of  $\mathcal{N} = 560 M_{\odot}$  Gyr. Here  $\tau_{\text{SN}}$  is the “effective” SN interval corrected by McKee to account for the

ineffectiveness in destroying dust of SN that go off inside superbubbles and out of the Galactic plane (some SN Ia’s). McKee (1989) estimates that these considerations reduce the effective SN rate by roughly a factor of 0.36. Recent determinations of the total ISM mass are substantially higher than the value from Scoville & Sanders (1987), which was used by McKee (1989). For example, Kalberla & Kerp (2009) give a value of  $12.5 \times 10^9 M_\odot$  with roughly a 15% uncertainty (Kalberla, private communication). A more recent determination of the global SN rate was carried out by Li et al. (2011) using a large database of galaxies in the local universe, and they found a value of  $2.84 \pm 0.60$  SN (including both types I and II) per century or an interval of 35 yr, which is a slightly shorter interval than McKee’s adopted value of 125 yr, after including his 36% correction factor. Combining these values, without McKee’s correction factor, yields a value of  $\mathcal{N} = 440 \pm 120 M_\odot$  Gyr. Including the correction factor this becomes  $\mathcal{N} = 1220 \pm 320 M_\odot$  Gyr which is significantly larger than found using McKee’s values.

Local estimates of the SN rate and surface density offer the possibility of a better estimate for the region of the Galaxy near the Sun, for which we have the best data on the dust content and size distribution, but at the expense of more uncertainty in the rates themselves. Estimates of the local values for  $\mathcal{R}_{\text{SN}}$  and  $\Sigma_{\text{ISM}}$ , have recently been made by Calura et al. (2010). For the SN rate per unit area (combining types I and II) they use results from Cappellaro (1996) and find  $\mathcal{R}_{\text{SN}} = 0.015 \pm 0.008 \text{ Gyr}^{-1} \text{ pc}^{-2}$ . This rate is based on the global rate per galaxy for nearby galaxies divided by an area of  $10^9 \text{ pc}^2$  for the Milky Way, making it a global average. However it is consistent with the local rate found by Schmidt et al. (2014) for the region within 600 pc of the Sun,  $\mathcal{R}_{\text{SN}} = 0.015^{+0.004}_{-0.003} \text{ Gyr}^{-1} \text{ pc}^{-2}$  for core collapse SN. Global SN II and SN I estimates (e.g. Li et al. 2011) find that the SN I rate is about a quarter of the SN II rate, so we increase the Schmidt et al. (2014) by 25%. The estimate of the mass per unit area in Calura et al. (2010) is  $10.5 \pm 3.5 M_\odot \text{ pc}^{-2}$ , which is a local surface density using results from Kulkarni & Heiles (1987), Dame (1993) and Olling & Merrifield (2001). Using the rate per unit area from Schmidt et al. (2014) (corrected for SN I) and surface density from Calura et al. (2010) without the SN rate correction factor yields  $\mathcal{N} = 560 \pm 240 M_\odot$  Gyr. With the SN rate correction factor we get  $\mathcal{N} = 1560 \pm 670 M_\odot$  Gyr.

## 4.2. Effects of the ISM Model

While the formulation of the problem above appears to be correct in a broad sense, several important factors are not explicitly taken into account. In particular, the morphology of the medium, i.e. such things as the degree of homogeneity and the assumed volume filling fractions for the different phases in the ISM, could strongly affect how SNRs interact with the ISM. The temporal and spatial correlation of SN may also be important. The simplest assumption is that the medium in which SN explosions occur is completely uniform in which case the value of  $M_g$  in equation 4 is simply taken directly from Eq. 2. However if we have a multi-phase medium, we must consider how the shock propagates in the different phases and the consequences for grain destruction per SNR.

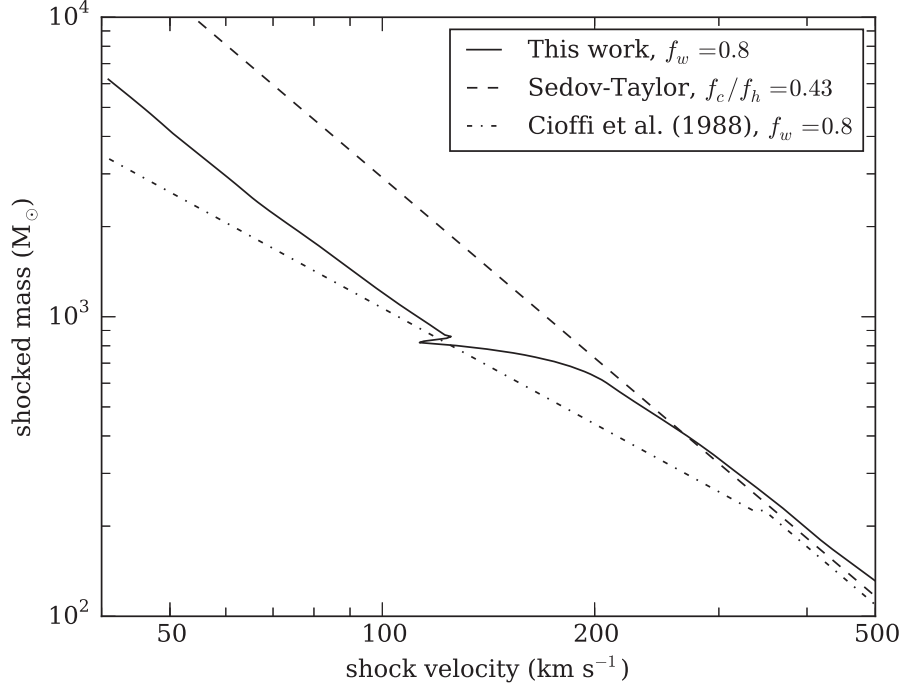


Fig. 8.— Comparison of the mass shocked to a given shock speed for our hydrodynamical calculations, the Sedov-Taylor evolution used in the hot gas dominated ISM model of McKee (1989) and the offset power law approximation of Cioffi et al. (1988). The McKee model (Sedov-Taylor) line is for an assumed a warm gas cloud filling factor of 0.3 and a hot gas filling factor of 0.7. For the results using our hydro calculations and the Cioffi et al. (1988) offset power law we assume a warm gas filling factor of 0.8. (The shocked mass is proportional to  $f_w$ .) The importance of the assumed shock expansion model is clear since the amount of dust destroyed is proportional to mass shocked (see text).

JTH96 used the method of Dwek & Scalo (1980) and McKee (1989) in which it is assumed that there is a high filling factor of hot gas and that the warm gas is confined to clouds embedded in the hot medium. In this picture the SNR shock expands quickly through the dominant low density hot phase, remaining adiabatic because of the low density. When clouds of warm gas are encountered, they are shocked, though the shock that propagates through the cloud is at a lower speed because of the higher density. The post-shock pressures inside and outside the cloud are roughly equal, which leads to a shock speed inside the cloud,  $v_{sc} \approx \sqrt{\rho_h/\rho_c} v_{sh}$ , where the subscript  $c$  is for clouds and  $h$  is for hot gas. The mass of cloud gas shocked to a given shock speed or higher is then given by  $M_s = f_c \rho_c V_s = (f_c/f_h) M_{ST}(v_{sc})$ , where  $M_{ST} = 6800 E_{51}^2 / v_{s7}^2 M_\odot$  is the mass shocked to at least  $v_{s7} = v_s/100 \text{ km s}^{-1}$  in the Sedov-Taylor phase of expansion,  $f_c$  is the filling factor of clouds (warm phase),  $f_h$  is the filling factor of hot gas and  $V_s$  is the volume contained in the shock. This



expression for the mass of gas shocked to a given speed is compared in Figure 8 with our results for our standard model. The resulting total mass of gas cleared of dust is then

$$M_g = \frac{f_c}{f_h} 13600 E_{51} \int \frac{\epsilon(v_s)}{v_{s7}^3} dv_{s7} \quad (5)$$

where  $\epsilon(v_s)$  is the grain destruction efficiency for a steady shock with speed  $v_s$ . In the figure we have used  $E_{51} = 1$  for the Sedov-Taylor expansion model whereas our standard model uses  $E_{51} = 0.5$ . The Cioffi et al. (1988) model curve uses their equations for the late time offset power-law expansion and the transition time between early Sedov-Taylor expansion and power-law expansion. We use  $E_{51} = 0.5$  for that curve. Both the curve for our model result and that for the Cioffi et al. (1988) model are multiplied by an assumed filling factor for warm gas of  $f_w = 0.8$  as discussed below.

Implicit in the above method result is the assumption that the presence of the clouds does not slow the expansion of the blast wave, which propagates at the S-T rate. Also assumed in this formulation is that shocks propagating into clouds are equivalent, in terms of grain destruction, to plane parallel steady shocks. This assumption may be questioned since the shocks are wrapping around clouds and enveloping them, which could lead to strongly non-steady effects.

The picture just described is essentially that of McKee & Ostriker (1977), who argued for a large filling factor of hot gas,  $\sim 70\%$ . The result of a large hot gas filling factor has been disputed for a number of reasons (e.g., Slavin & Cox 1992; Ferrière 1998, see discussion below) including the fact that the hot bubbles created by SNRs are considerably smaller when the magnetic field is included and that a substantial fraction of SNRs are spatially and temporally correlated, which decreases their effectiveness in filling the medium with hot gas. Though McKee took this latter effect into account in his estimate of grain destruction, its effect on the hot gas filling factor was not considered.

Our calculation of grain destruction in an evolving SNR assumes a different picture from that assumed by JTH96 and Bocchio et al. (2014) to derive dust destruction timescales. Here we have assumed a uniform density, effectively assuming that  $f_w \gg f_h$ , where  $f_w$  is the filling factor for the warm medium, no longer assumed to be confined to clouds. We speculate that if a remnant runs into a region of hot gas that has a pressure not too different from that inside the remnant, then the rest of the remnant will continue to expand as it would in a uniform medium. In that case, the only difference would be that  $M_g$  in equation 4 would need to be multiplied by a factor of  $f_w$ , if we assume that the part of the shock front that propagates into the hot region does not effectively destroy any dust. This seems reasonable since the shock from a remnant impinging on a pre-existing hot bubble will in most cases decay into a sound wave before encountering a bubble wall. The shocked mass for our hydro calculation plotted in Figure 8 includes the factor  $f_w$  set to 0.8.

### 4.3. Volume Filling Factors in the ISM

The volume filling factors for the warm and hot phases of the ISM have yet to be determined in any definitive way. Ferrière (1998) has carried out probably the most comprehensive study using a range of observational results and theoretical considerations to arrive at the filling factors of the various phases of the ISM (see also Ferrière 2001). She found that in the solar neighborhood the warm gas fraction, including both neutral and ionized phases, is close to 80%. In her work as well as that of others, the filling factors of the different phases vary substantially as a function of galactic radius and height above the plane. For the most part, though in regions near the galactic radius of the Sun and near the Galactic plane, the filling factor for the hot phase is  $\lesssim 20\%$ . Other theoretical attempts have centered around large scale numerical hydrodynamical or magneto-hydrodynamical calculations (e.g., de Avillez & Breitschwerdt 2005; de Avillez et al. 2012; Hill et al. 2012), though achieving sufficient spatial resolution remains challenging. Most of these studies in recent years have found modest filling factors for the hot gas  $\lesssim 20\%$ , but also for the warm gas,  $f_w \sim 20\text{--}50\%$ . Often a substantial fraction of the volume is in the thermally unstable temperature range of  $10^4\text{--}10^{5.5}$  K. This occurs in these simulations because of the amount of turbulence injected by SNRs.

In addition to the resolution issues faced by these simulations, the heating and cooling rates are often included in very approximate ways. Since these rates depend on a range of factors including dust content and the local ionizing radiation field, the filling factor for warm gas is particularly difficult to simulate. Given these considerations, we take as an upper limit 80% as the filling factor of the warm gas. We assume that there is no significant grain destruction in the other 20% of the medium that the SNR shock overruns, which includes cold, dense gas and hot gas.

### 4.4. Dust Destruction Timescales

Combining the data on ISM mass and SN rate with modeled SNR evolution and dust destruction, the dust destruction timescale is

$$\tau_{\text{dust}} = \frac{\mathcal{N}}{\delta_{\text{SN}} M_{g,\text{eff}}} \quad (6)$$

where  $\mathcal{N}$  is the SN mass interval,  $\delta_{\text{SN}}$  is the correction factor intended to account for the effects of correlated SN and SN out of the plane (which McKee estimates to be 0.36 as discussed above) and  $M_{g,\text{eff}}$  is the effective mass of gas cleared of dust per SN including the effects of the inhomogeneous ISM. As discussed above, for the warm gas dominated ISM,  $M_{g,\text{eff}} = f_w M_g$ , where  $M_g$  is calculated for an SNR going off in a homogeneous warm medium (see table 2). For the hot medium (HIM in the terminology of McKee & Ostriker 1977) dominated case, we can use the methodology of Dwek & Scalo (1979) and McKee (1989) as discussed in §4.2, with  $M_g$  calculated by equation 5. Our results are summarized in Table 3.

The dust destruction timescales listed in the table are substantially higher than those found by JTH96, 0.37 Gyr for silicate and 0.63 Gyr for carbonaceous dust. The factor of 4 to 5 increase

is due primarily to the increase of a factor of  $\sim 3$  in the SN mass interval, which in turn derives from a higher estimate for the ISM mass or surface density. Another important factor is the use of a lower SN explosion energy ( $5 \times 10^{51}$  ergs rather than  $10^{51}$  ergs), which lowers the estimate of  $M_{g,\text{eff}}$  by roughly a factor of 2 whether one assumes a HIM dominated medium or a warm gas dominated medium. Using the same values as JTH96, including our  $E_{51} = 1$  calculation, would lead to dust destruction timescales roughly the same as those of JTH96. Nevertheless, while the effective SN explosion energy (after early cosmic ray losses) is still quite uncertain, it seems clear that the value from McKee (1989) for the ISM mass is low. In addition the values in Table 3 use  $f_w = 0.8$ , which is likely to be an upper limit. A lower value for  $f_w$  will decrease the effectiveness of SNR grain destruction, increasing the dust destruction timescale.

For comparison with the destruction timescale, recent estimates for the grain production timescale center around  $2.5 \times 10^9$  yr (Jones & Tielens 1994). Using the simple estimate of grain equilibrium fraction of McKee (1989),  $\delta_{\text{eq}} = \delta_{\text{in}}[1 + t_{\text{in}}/\tau_{\text{dust}}]^{-1}$ , where  $t_{\text{in}}$  is the dust injection timescale and  $\delta_{\text{in}}$  is the mass fraction in dust when injected into the ISM, our standard run destruction timescale values leads to only about 30–40% of the silicate elements and 45–50% of the carbon locked up in grains in contrast to derived values of  $\sim 90\%$  and  $\sim 50\%$  for the depletion of silicate and carbon grain constituents in the diffuse ISM. (We have followed JTH96 in assuming  $\delta_{\text{in}} = 0.9$ .) Thus with these results we can explain the carbon depletion fraction but still fall short of explaining the silicate depletions. However, with the higher carbonaceous grain sputtering yields advocated by Serra Díaz-Cano & Jones (2008), the carbonaceous grain destruction timescales would also be too short.

The discrepancy between the rates of dust production and destruction can also be illustrated by considering the net effects of SNe on the dust content in the ISM. The rate of grain destruction by SNRs depends on the dust-to-gas mass ratio of the ISM into which the remnant is expanding. Our results show that, for a gas-to-dust ratio of 163, a typical SNR destroys  $\sim 3.7 M_{\odot}$  of silicate dust and  $\sim 1.4 M_{\odot}$  of carbonaceous dust (using our standard model results). Core collapse supernovae (CCSN) produce at most 0.1–0.2  $M_{\odot}$  of dust (Gomez et al. 2012; Arendt et al. 2014; Temim et al. 2015), so if the ISM has roughly solar metallicity (in gas and dust), SNe are net destroyers of dust. This discrepancy cannot be made up by dust production in low mass stars. For a Salpeter IMF, the number of the most efficient dust producing AGB stars, with initial masses in the 2–4  $M_{\odot}$  range, is about 4 times higher than the number of stars massive enough to become CCSN, but their dust yield is only  $\sim 0.01 M_{\odot}$  (Ventura et al. 2014). Thus the relative ratios between the rates of grain destruction by SNRs, and production by CCSN and AGB stars is approximately 100:4:1, respectively. This discrepancy demands that either a large fraction of the dust is shielded in some way, or that not all SNe are as efficient in destroying the dust as estimated (e.g. because of correlated SNe) or that dust is created in the ISM (e.g. via accretion). Because the discrepancy is so large, all of these effects likely come into play.

Table 3. Grain Destruction Timescale Estimates (Gyr)<sup>a</sup>

ISM model <sup>b</sup>	SN mass interval sources	
	Local	Global
Carbonaceous grains		
HIM dominated	$1.6 \pm 0.7$	$1.2 \pm 0.3$
WM dominated	$3.2 \pm 1.4$	$2.6 \pm 0.7$
Silicate grains		
HIM dominated	$0.92 \pm 0.39$	$0.72 \pm 0.20$
WM dominated	$2.0 \pm 0.8$	$1.5 \pm 0.4$
SN mass interval <sup>c</sup> ( $\mathcal{N}$ in Gyr $M_{\odot}$ )		
	$560 \pm 240$	$440 \pm 120$

<sup>a</sup>The timescale estimates depend directly on the SN mass interval listed in the last line of the table. The errors are from the estimated errors in the SN mass interval only.

<sup>b</sup>The HIM dominated values are for the assumption that the grain destruction occurs in warm clouds embedded in a hot medium as in Eq. 5 and using the plane parallel steady shock model results for  $M_g$  with  $f_c/f_h = 0.43$ . The WM dominated values use the hydro results for our standard model with the  $M_g$  calculated as in Eq. 2 multiplied by  $f_w = 0.8$ .

<sup>c</sup>The SN correction factor,  $\delta_{\text{SN}} = 0.36$ , is not included in the values for  $\mathcal{N}$  given in the table but is included in the timescale values.

## 5. Conclusions

We have evaluated the destruction of interstellar dust grains in supernova remnants evolving in a homogeneous, magnetized ISM. We find that the grain destruction efficiency is not very different from that calculated for steady, plane parallel shocks with the same shock parameters as the evolving spherical shocks except for  $v_s \gtrsim 200$ . Our efficiency calculations have been carried to lower and higher shock speeds than the previous steady shock calculations.

Recent grain destruction calculations have used the results of the grain destruction efficiency in the context of a hot gas dominated ISM (JTH96, Bocchio et al. 2014). When we use our results self-consistently, that is assuming that the medium is dominated by warm gas, we find grain destruction timescales that are larger than those found previously, e.g. for our standard run with an explosion energy of  $5 \times 10^{50}$  ergs, using the local estimates of SN rates and mass per unit area yields  $\tau_{\text{dust}} = 2.0$  Gyr and 3.2 Gyr for silicates and carbonaceous grains respectively. This does not entirely remove the problem of a destruction timescale that is too short relative to the creation timescale to account for the level of elemental depletion in the ISM, but does mitigate the situation. If the volume filling factor of warm ISM is smaller than our assumed upper limit of 80% and SNR grain destruction is inefficient in the other phases of the ISM, then these timescale estimates will increase as  $1/f_w$ . We note that there are many uncertainties that we have not discussed in this paper concerning both grain destruction and creation as discussed at length in Jones & Nuth (2011). Our results demonstrate the importance of the morphology of the ISM, in particular the type of medium into which SNRs typically evolve, for determining dust destruction timescales.

This research was supported by NASA Astrophysics Theory Program grant NNX12AF84G. ED acknowledges support by NASA Astrophysical Data Analysis Program ADAP13-0094. We thank John Raymond for providing the steady shock model calculations and our collaborator Xander Tielens for helpful discussions. We also wish to thank the developers of matplotlib, a python plotting library, which we used to produce all of the plots in this paper.

## REFERENCES

- Arendt, R. G., Dwek, E., Kober, G., Rho, J., & Hwang, U. 2014, *ApJ*, 786, 55
- Balsara, D. S., Bendinelli, A. J., Tilley, D. A., Massari, A. R., & Howk, J. C. 2008, *MNRAS*, 386, 642
- Bocchio, M., Jones, A. P., & Slavin, J. D. 2014, *A&A*, 570, A32
- Calura, F., Recchi, S., Matteucci, F., & Kroupa, P. 2010, *MNRAS*, 406, 1985
- Cappellaro, E. 1996, in *IAU Symposium*, Vol. 171, *New Light on Galaxy Evolution*, ed. R. Bender & R. L. Davies, 81

- Chevalier, R. A. 1974, *ApJ*, 188, 501
- Cioffi, D. F., McKee, C. F., & Bertschinger, E. 1988, *ApJ*, 334, 252
- Colella, P., & Woodward, P. R. 1984, *Journal of Computational Physics*, 54, 174
- Cowie, L. L., & McKee, C. F. 1977, *ApJ*, 211, 135
- Cox, D. P. 1972, *ApJ*, 178, 159
- Cox, D. P., & Raymond, J. C. 1985, *ApJ*, 298, 651
- Crank, J., & Nicolson, P. 1996, *Advances in Computational Mathematics*, 6, 207
- Dame, T. M. 1993, in *American Institute of Physics Conference Series*, Vol. 278, *Back to the Galaxy*, ed. S. S. Holt & F. Verter, 267–278
- de Avillez, M. A., Asgekar, A., Breitschwerdt, D., & Spitoni, E. 2012, *MNRAS*, 423, L107
- de Avillez, M. A., & Breitschwerdt, D. 2005, *A&A*, 436, 585
- Draine, B. T., & Salpeter, E. E. 1979a, *ApJ*, 231, 438
- . 1979b, *ApJ*, 231, 77
- Dwek, E. 1981, *ApJ*, 247, 614
- Dwek, E., Foster, S. M., & Vancura, O. 1996, *ApJ*, 457, 244
- Dwek, E., & Scalo, J. M. 1979, *ApJ*, 233, L81
- . 1980, *ApJ*, 239, 193
- Ferrière, K. 1998, *ApJ*, 503, 700
- Ferrière, K. M. 2001, *Reviews of Modern Physics*, 73, 1031
- Gomez, H. L., et al. 2012, *ApJ*, 760, 96
- Grevesse, N. 1984, in *Frontiers of Astronomy and Astrophysics*, ed. R. Pallavicini, 71
- Hill, A. S., Joungh, M. R., Mac Low, M.-M., Benjamin, R. A., Haffner, L. M., Klingenberg, C., & Waagan, K. 2012, *ApJ*, 750, 104
- Jones, A. P., Fanciullo, L., Köhler, M., Verstraete, L., Guillet, V., Bocchio, M., & Ysard, N. 2013, *A&A*, 558, A62
- Jones, A. P., & Nuth, J. A. 2011, *A&A*, 530, A44

- Jones, A. P., & Tielens, A. G. G. M. 1994, in *The Diffuse Interstellar Bands*, ed. A. G. G. M. Tielens, 79–83
- Jones, A. P., Tielens, A. G. G. M., & Hollenbach, D. J. 1996, *ApJ*, 469, 740
- Jones, A. P., Tielens, A. G. G. M., Hollenbach, D. J., & McKee, C. F. 1994, *ApJ*, 433, 797
- Kalberla, P. M. W., & Kerp, J. 2009, *ARA&A*, 47, 27
- Kulkarni, S. R., & Heiles, C. 1987, in *Astrophysics and Space Science Library*, Vol. 134, *Interstellar Processes*, ed. D. J. Hollenbach & H. A. Thronson, Jr., 87–122
- Li, W., Chornock, R., Leaman, J., Filippenko, A. V., Poznanski, D., Wang, X., Ganeshalingam, M., & Mannucci, F. 2011, *MNRAS*, 412, 1473
- Mathis, J. S., Rumpl, W., & Nordsieck, K. H. 1977, *ApJ*, 217, 425
- McKee, C. 1989, in *IAU Symposium*, Vol. 135, *Interstellar Dust*, ed. L. J. Allamandola & A. G. G. M. Tielens, 431
- McKee, C. F., Hollenbach, D. J., Seab, G. C., & Tielens, A. G. G. M. 1987, *ApJ*, 318, 674
- McKee, C. F., & Ostriker, J. P. 1977, *ApJ*, 218, 148
- Olling, R. P., & Merrifield, M. R. 2001, *MNRAS*, 326, 164
- Raymond, J. C., & Smith, B. W. 1977, *ApJS*, 35, 419
- Schmidt, J. G., Hohle, M. M., & Neuhäuser, R. 2014, *Astronomische Nachrichten*, 335, 935
- Scoville, N. Z., & Sanders, D. B. 1987, in *Astrophysics and Space Science Library*, Vol. 134, *Interstellar Processes*, ed. D. J. Hollenbach & H. A. Thronson, Jr., 21–50
- Seab, C. G., & Shull, J. M. 1983, *ApJ*, 275, 652
- Serra Díaz-Cano, L., & Jones, A. P. 2008, *A&A*, 492, 127
- Shull, J. M. 1977, *ApJ*, 215, 805
- Shull, J. M., & McKee, C. F. 1979, *ApJ*, 227, 131
- Siebenmorgen, R., Voshchinnikov, N. V., & Bagnulo, S. 2014, *A&A*, 561, A82
- Slavin, J. D., & Cox, D. P. 1992, *ApJ*, 392, 131
- . 1993, *ApJ*, 417, 187
- Slavin, J. D., Jones, A. P., & Tielens, A. G. G. M. 2004, *ApJ*, 614, 796



- Temim, T., Dwek, E., Tchernyshyov, K., Boyer, M. L., Meixner, M., Gall, C., & Roman-Duval, J. 2015, *ApJ*, (in press, arXiv:1411.4574)
- Ventura, P., Dell’Agli, F., Schneider, R., Di Criscienzo, M., Rossi, C., La Franca, F., Gallerani, S., & Valiante, R. 2014, *MNRAS*, 439, 977
- Weingartner, J. C., & Draine, B. T. 2001, *ApJ*, 548, 296
- Weingartner, J. C., Draine, B. T., & Barr, D. K. 2006, *ApJ*, 645, 1188
- Zubko, V., Dwek, E., & Arendt, R. G. 2004, *ApJS*, 152, 211